Energy &
Environmental
Science

ROYAL SOCIETY
OF CHEMISTRY

PAPER

View Article Online
View Journal | View Issue

Check for updates

Cite this: *Energy Environ. Sci.*, 2020, **13**, 3646

Solar passive distiller with high productivity and Marangoni effect-driven salt rejection†

Matteo Morciano,[abc] Matteo Fasano,*[ab] Svetlana V. Boriskina,[c] Eliodoro Chiavazzo*[a] and Pietro Asinari*[ad]

Received 7th May 2020,
Accepted 7th August 2020

DOI: 10.1039/d0ee01440k

rsc.li/ees

Inadequate water supply, sanitation and hygiene in remote locations, developing countries, and disaster zones fuel the growing demand for efficient small-scale desalination technologies. The aim is to provide high-quality freshwater to water-stressed and disaster-stricken communities even in the absence of energy infrastructure. The major key drivers behind the development of these technologies are the low cost of materials, the flexibility of the technology, the sustainability of the freshwater production, and the long-term stability of the device performance. However, the main challenge is to achieve stable performance by either preventing or mitigating salt accumulation during the desalination process. We present a multistage passive solar distiller whose key-strength is an optimized geometry leading to enhanced water yield (as compared to similar state of the art technologies) and spontaneous salt rejection. A comprehensive theoretical study is conducted to explain the apparently paradoxical experimental effective transport exceeding classical diffusion by two orders of magnitude. In our study, the Marangoni effect is included at the water–air interface and it stems from spatial gradients of surface tension. Interestingly, theoretical and experimental results demonstrate that the device is able to reject overnight all the salt accumulated on each evaporator during daytime operation. Furthermore, under realistic conditions, a distillate flow rate of almost 2 L m^{-2} h^{-1} from seawater at less than one sun illumination has been experimentally observed. The reported mechanism of the enhanced salt rejection process may have tremendous implications in the desalination field as it paves the way to the design of a new generation of hydrophilic and porous materials for passive thermal desalination. We envision that such a technology can help provide cheap drinking water, in a robust way, during emergency conditions, while maintaining stable performance over a long time.

Broader context

In the broad field of passive solar desalination, the Achilles' heel of the technologies is crystallization of salt particles on the photothermal component and device clogging. Addressing this issue is of primary importance to maintain uninterrupted operation with stable water evaporation rates. Recently, new nanostructured materials with anti-clogging properties have been proposed to limit the salt accumulation. However, the high cost of the nanostructured materials and the difficulty of scaling up the prototypes hindered their widespread adoption. Here, we investigated thoroughly the mechanisms underlying the salt particles transport, with the aim to understand and improve the salt rejection processes. The main achievement of our research work lies in the fundamental understanding of the relationship between the so-called Marangoni effect and the efficient and enhanced salt rejection. The role of Marangoni effect in the salt rejection process taking place in passive desalination technologies has never been investigated before. Our experiments show that, as a result of the Marangoni effect, a 75% salt concentration decrease is achieved after 2 hours. We suggest that this effect may have tremendous implications in the design of a new generation of hydrophilic and porous material for desalination devices with enhanced and tailored salt rejection properties.

1 Introduction

Global warming and clean water scarcity are progressively impacting economies and societies. International collaborative efforts have taken place to limit global temperature rise and address clean water scarcity in the most water-stressed areas, where nearly two-thirds of global population will live by the year 2025.[1–4]

---

[a] *Department of Energy, Politecnico di Torino, Corso Duca degli Abruzzi 24, 10129 Torino, Italy. E-mail: eliodoro.chiavazzo@polito.it, matteo.fasano@polito.it, pietro.asinari@polito.it*
[b] *Clean Water Center, Politecnico di Torino, Corso Duca degli Abruzzi 24, 10129 Torino, Italy*
[c] *Department of Mechanical Engineering, Massachusetts Institute of Technology, Cambridge, Massachusetts 02139, USA*
[d] *INRIM Istituto Nazionale di Ricerca Metrologica, Strada delle Cacce 91, Torino 10135, Italy*

† Electronic supplementary information (ESI) available. See DOI: 10.1039/d0ee01440k

In this context, flexible (*i.e.* accessible to more people), robust, efficient and stand-alone (where no moving parts are present) desalination technologies able to operate even in emergency conditions have been recently designed and studied in literature.[5–21] The attention has been mainly focused on the study and design of new nano-structured materials and smart structures able to improve the solar-to-vapour conversion and the energy management.[13,22–29] In 2018 some of the authors proposed a solar passive and multistage distiller[5] able to achieve performance beyond the thermodynamic limit of a single stage device, by recovering the latent heat of condensation. The importance of recovering the latent heat of condensation in passive distillation devices has been then extensively discussed and emphasized by Wang and co-workers,[30] and Pang and co-workers.[31] In both the article reviews, the authors state that high-performance cannot be achieved without efficient condensation, accompanied by the recovery of the latent heat of condensation. Afterwards, Xu and co-workers[13] proposed a solution to optimize the overall heat and mass transfer in a thermally localized multistage solar still. According to their investigation, a 10-stage prototype achieved a solar-to-vapour conversion efficiency of 385% relying on solar heat localization and latent heat recycling. The solar heat localization and the latent heat of condensation recovery have been also exploited to prototype portable systems able to produce fresh water and generate electricity simultaneously. In 2019, Wang and co-workers proposed a photovoltaic-membrane multistage distillation device.[10] In detail, the PV panel – coupled with the distillation device – was employed as both photovoltaic component for generating electricity (efficiency higher than 11%, which is comparable with the one achieved without the membrane distillation device installed at the back side of the PV panel) and photothermal component for producing freshwater. It is worth noting that this coupling can be obtained by embedding the distillation device in already existing electricity power plants, thus avoiding additional land consumption.

Although interesting, most of these passive solutions are still not able to ensure long-term stability of performance. In fact, one of the major and unresolved issues affecting passive desalination devices is the degradation of performance over time due to salt accumulation and clogging. During operating conditions, vaporization occurs and accumulated salt particles have to be properly discharged to keep constant the distillate flow rate.[32,33] To overcome this limit, a fouling mitigation strategy based on rinsing procedure was suggested for the multistage distiller in ref. 5, thus allowing to ensure durable distillation performances that, after the first day of test, stabilized around a limited 15% productivity reduction. Moreover, several prototypes able to perform a directional salt crystallization have been recently proposed in literature. In 2018, Shi and co-workers fabricated a 3D cup shaped solar evaporator able to achieve Zero Liquid Discharge (ZLD) desalination.[34] The key idea is to rationally separate the solar absorbing surface from the salt crystallization surface. In detail, the lateral and vertical surfaces of the 3D cup are affected by the salt accumulation; whilst, the horizontal evaporating surface at the bottom of the cup remains free of accumulated salt particles. Therefore, the performance of the device did not experience a noticeable decay with time. The reason is that different evaporation rates take place, because of both the different humidity on the surfaces of the cup and the vicinity to the water feeding channel. The same year, also Xia and co-workers[33] addressed this challenge by proposing a novel design through which the crystallisation sites (edges of the structure) of the salt particles were spatially isolated from the water evaporation surface, thus achieving continuous vapour generation. In detail, the edge of the evaporating surface showed higher concentration than the inner part, because of the combined effect of the evaporation ability and the capillarity of the hydrophilic component. In addition to this, the proposed device was able to perform gravity-assisted salt harvesting.

Furthermore, Kashyap and co-workers proposed a new efficient and flexible porous material with anti-clogging characteristics.[35] The anti-clogging property of the material was achieved through tailored pore size and coating of poly(3,4-ethylenedioxythiophene)–poly(styrenesulfonate) (PEDOT–PSS) on the surface where heat localization occurs. However, the development of such materials may not represent the optimal approach when dealing with emergency conditions, since cost-effective solutions are required. A significant advance in this direction was proposed by Ni and co-workers,[6] where an easier and more efficient fouling mitigation strategy was conceived and extensively studied. In detail, this work proposed a passive floating solar still appropriately designed to reject all the salt in few hours relying on an optimized ratio between salt rejecting and evaporating areas, but limited distillate productivity. However, no theoretical explanation was reported and this prevents to rationalize and to generalize the proposed solution.

In this work, for the first time, we rationalize the salt rejection enhancement and we optimize both the distillate productivity and the salt rejection in passive solar desalination systems, as confirmed also experimentally. Here, we suggest that the gradient of the surface tension due to salinity concentration gradient at the interface between saltwater and air represents an additional driving force for moving solvent and salt particles.[36] The gradient of the surface tension along this interface creates tangential shear forces and, as a result, a slip velocity appears. Therefore, the saltwater solution is driven to flow from low surface tension towards higher one. This phenomenon, called Marangoni effect,[37] which has been previously observed in various processes like welding,[38] electron beam melting[39] and crystal growth,[40] plays an important role in the salt rejection mechanism observed in our experiments. While this phenomenon is well-know and widely investigated in literature,[36,37,41] the Marangoni effect has never been exploited so far in the field of passive desalination. Moreover, the development of the prototype has been carried out with attention to enhanced yield and cost reduction for approaching practical applications.

2 Structure and design of the modular solar distiller

The modular distiller is able to passively produce freshwater from saltwater by exploiting thermal energy.[5] The working

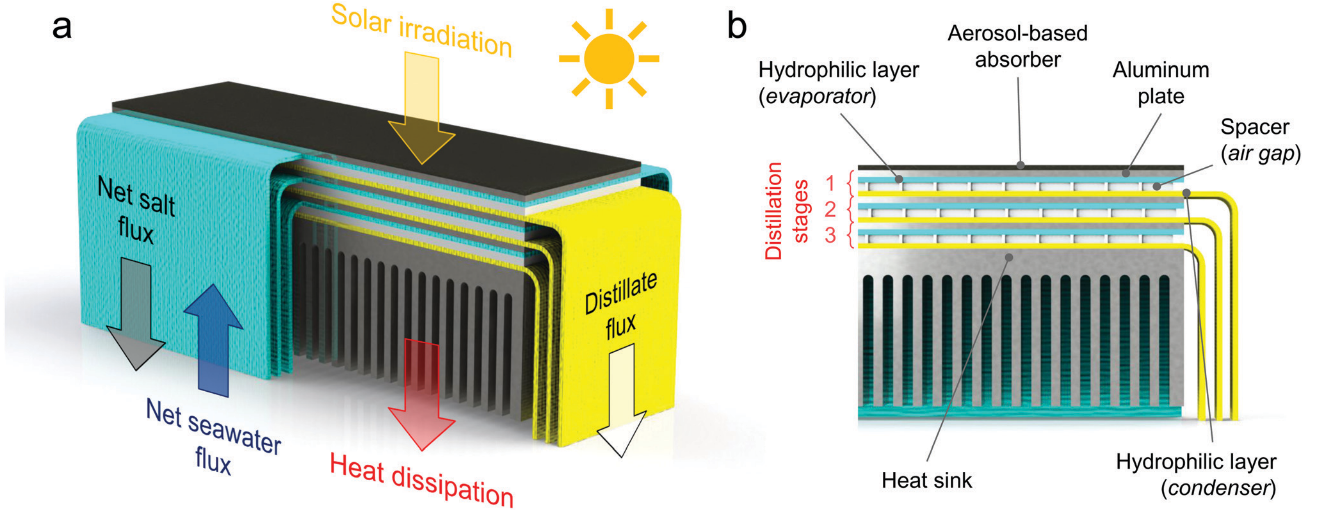

Fig. 1 Illustrative 3-stage configuration device: working principle during daylight operating hours. (a) Isometric view and (b) detail of a section along the lengthy side. Seawater (blue arrow) is provided to each stage of the device by capillary action exerted by the cyan hydrophilic layers (evaporators). After that, solar radiation (yellow arrow) is converted into thermal energy by a aerosol-based absorber placed on top of the device. The thermal energy drives multiple evaporation and condensation processes through each spacer and then it is rejected to the environment through the heat sink. Distilled water (white arrow) condenses on each yellow hydrophilic layer (condenser) and it is collected in a basin by gravity. The gray arrow represents the Marangoni-driven net salt flux, which is aided by the enhanced ratio between salt rejecting and evaporating areas. Note that, in the picture reported in panel a, for the sake of clarity and simplicity, the hydrophilic layers (evaporator side) are hidden for half of their length.

principle discussed here is schematized in Fig. 1. Saltwater rises through the hydrophilic layers (labeled as evaporators) because of the capillary forces. Thus, no moving parts or active components are installed. Solar radiation is absorbed on the top of the first stage of the device by the black absorber, which heats the saltwater in the evaporator (see Supplementary Note 1 and Fig. S1a, ESI†). A temperature difference is thus established across an air gap created by a spacer between the evaporator and another hydrophilic layer, which is labeled as condenser (see Fig. S1b and c, ESI†). Such temperature difference provides a vapour pressure difference, thus driving a net vapour flux from the evaporating to the condensing layer. The distilled water accumulated in the condenser is discharged into a distillate basin by gravity, through some protruding strips. The vapour condensation on the hydrophilic layer releases latent heat, which is employed to drive further distillation processes in the successive stages. A heat sink is installed at the bottom of the stack to reject the heat into the saltwater basin (see Fig. S1d, ESI†). It is worth to point out that each vaporization/condensation process occurs at ambient total pressure.

Each distillation stage is delimited by two aluminum plates of 12×3.5 cm^2. Those aluminum plates (thickness $\approx$ 1 mm) are used for supporting the hydrophilic layers (namely evaporator and condenser) and ensuring robustness. A thin plastic film (linear low-density polyethylene – LLDPE) is interposed between each hydrophilic layer containing saltwater and the aluminum plate, to mitigate a possible crystallization of salt on the metal during operations. The aluminum plates can efficiently recover the latent heat of condensation because of their high thermal conductivity.

Seawater reaches the horizontal portion of each evaporator *via* two sides, thus speeding up the feeding process and increasing the section available for the salt rejection. The width of the strips through which seawater is supplied by capillary action to each evaporator is 12 cm; whereas, the horizontal extension of the hydrophilic layers (evaporating portion) is equal to the size of the aluminum plates, namely 3.5 cm. Therefore, the longest path that the salt particles have to travel to reach the border and flow back into the sea is half the width of the evaporating surface, that is $\approx$1.75 cm (see Supplementary Note 2, ESI†). Note that input and output strips are not directly exposed to air during experiments: each strip is covered by a LLDPE film to suppress natural vaporization towards the surrounding ambient (see Fig. S1, ESI†).

The hydrophilic layers (synthetic microfiber, see Supplementary Note 3 for their experimental characterization, ESI†) are separated by an air gap kept by a porous plexiglass frame. The porous structure of this spacer is obtained using a laser cutting machine. The thickness of this air gap ($\approx$1.65 mm) is properly selected for increasing the distillate flow rate while avoiding, at the same time, contamination between evaporator and condenser (see Supplementary Note 3 for details, ESI†). Further details on the experimental characterization of the solar absorber and the heat sink are also reported in Supplementary Note 3 (ESI†).

Note that, contrarily to traditional solar stills where the optical transmittance of the transparent cover may be reduced by condensed water drops, here the condensation process does not affect the optical performance of the device.

3 Results and discussion

3.1 Rejecting the salt

The salt rejection process is investigated by means of extensive experimental campaigns and numerical simulations. This study is referred to dark conditions, *i.e.* without considering the solar irradiance and evaporation, since the salt rejection takes place mainly during nighttime. In fact, during daytime the saltwater solution goes from the saltwater basin to each evaporator because of the evaporation process, which drives the capillary flow. At the same time, the vapour generation from saltwater leads to salt accumulation in the hydrophilic layers used as evaporators. However, we did not observe the formation of any salt crust layer during the 8 hours tests of evaporation, which mimic a typical daylight duration. During these tests, the observed experimental performance already considers salt accumulation and its possible detrimental effect on evaporation; however, no appreciable decay in the evaporation rate has been noticed during the 8 hours of test (see Supplementary Note 4, ESI†).

Based on the achieved results, we propose that Marangoni effect is responsible of the observed enhanced salt flow. This effect results from a gradient of surface tension at the interface between two phases. The surface tension typically changes due to variations in solute concentration, surfactant concentration, or temperature along the interface. When the concentration is responsible for variation of the surface tension, this effect is also know as soluto-capillary effect, whilst in cases where the surface tension varies with the temperature, it is called thermo-capillary effect.[40] Both effects can take place simultaneously. Here, the surface tension gradient is associated to a salt concentration gradient. It induces localized viscous stresses because of the resulting asymmetric interactions experienced by the molecules at the interface. Then, an interfacial flow, directed from the lower surface tension regions to the higher ones, takes place (see Supplementary Note 5, ESI†).[36]

3.1.1 Experimental procedure.

An experimental campaign focused on the ability of the device to reject the salt accumulated in the hydrophilic evaporator during the distillation process is performed. The fluid flow and solute transport in the hydrophilic layer (evaporator side) is investigated by monitoring the salt concentration in the porous medium over time.

First, a concentrated NaCl solution (200 g l^{-1}) is injected in the horizontal portion of the evaporator in Fig. 2a. Then, the vertical strips able to transport seawater to the evaporator are immersed in a basin filled with a solution mimicking seawater (salinity of the NaCl solution 35 g l^{-1}). As a result, the salt particles tend to diffuse back from the evaporator to the basin, similarly to the nighttime conditions of the distillation prototype. During the salt-rejection tests, the hydrophilic layer is supported by a plastic box, which is not represented in Fig. 2a for clarity.

A precision pipette and a digital refractometer are used to monitor the salt concentration in the porous medium with time. Three samples of solution $c_1(t)$, $c_2(t)$ and $c_3(t)$ are extracted from the main axis of the layer, which represents the most unfavorable area for the salt rejection mechanism (see Fig. 2a). The values $c_1(t)$, $c_2(t)$ and $c_3(t)$ are then averaged as $c(t) = [c_1(t) + c_2(t) + c_3(t)]/3$. This process is carried out for ten consecutive hours, with sampling every 1 hour. Note that the sampling could influence the evolution of the concentration profiles over time, therefore one single extraction is performed each time step. Then, to ensure repeatability and consistency of the results, the experiments (with the same initial and boundary conditions) are repeated five times over different days, and results averaged. Moreover, we highlight that the sample volume required by the refractometer to quantify the salinity can be as small as 2 metric drops (100 μl namely 0.1 g). Considering that each hydrophilic layer contains approximately 15 g of water (evaluated by considering the sizes and the porosity of the hydrophilic sample), this means that each extraction accounts for less than 0.7% of the total mass contained in the hydrophilic layer.

The obtained experimental measures are shown in Fig. 2b (see red circles, where the average $c(t)$ in the hydrophilic layer is reported *vs.* the duration of the salt-rejection test). The bars reported for each point show the minimum and maximum of the experimental measurements among the five repetitions. A 75% concentration decrease is experimentally observed after 2 hours; whilst, after ≈ 4 hours, the device is able to passively reject the salt accumulated during the daytime operations and to reach the equilibrium with seawater.

3.1.2 Numerical simulations.

In parallel with the experimental campaign, COMSOL Multiphysics simulations are performed to interpret the experimental results (see Fig. 2c and Supplementary Note 6 for further details, ESI†).

The procedure consists of two steps: (i) simulating the Marangoni flow and the purely diffusive flow separately, to quantify the effective diffusion coefficient by difference, (ii) using this value and the Darcy equation to reproduce the salt transport in the porous media, which is the hydrophilic layer.

First, the Navier–Stokes equations and the transport of diluted species are coupled and solved numerically to investigate the advection–diffusion phenomenon in presence of an interface with varying salt concentration gradient. The Navier–Stokes momentum equation is expressed as

$$\frac{\partial \rho \mathbf{u}}{\partial t} + \mathbf{u} \cdot \nabla(\rho \mathbf{u}) = -\nabla p + \nabla \cdot \left(\mu\left(\nabla \mathbf{u} + (\nabla \mathbf{u})^T\right) - \frac{2}{3}\mu(\nabla \cdot \mathbf{u})\mathbf{I} \right), \tag{1}$$

where ρ is the fluid density, which varies linearly with the solute concentration (see Supplementary Note 6, ESI†); $\mathbf{u}$ is the velocity vector of the fluid; p and μ the pressure and the viscosity, respectively. The transport of diluted species is instead modelled as

$$\frac{\partial c_i}{\partial t} + \nabla \cdot (-D_i \nabla c_i) + \mathbf{u} \cdot \nabla c_i = 0, \tag{2}$$

where c_i is the mass concentration of species i (namely, the mass of solute with respect to the total mass of solution) and D_i the molecular diffusion coefficient.

The simulation domain consists of a saltwater thin film of thickness equal to 1 mm (namely the thickness of the hydrophilic layer, δ_l) and length (L) equal to 17.5 mm (namely half of the horizontal portion of the evaporator, because of the symmetry). When the Marangoni effect is considered, a slip condition is applied at the top boundary of the domain to take into account the velocity of the solution at the liquid–air interface, which arises from

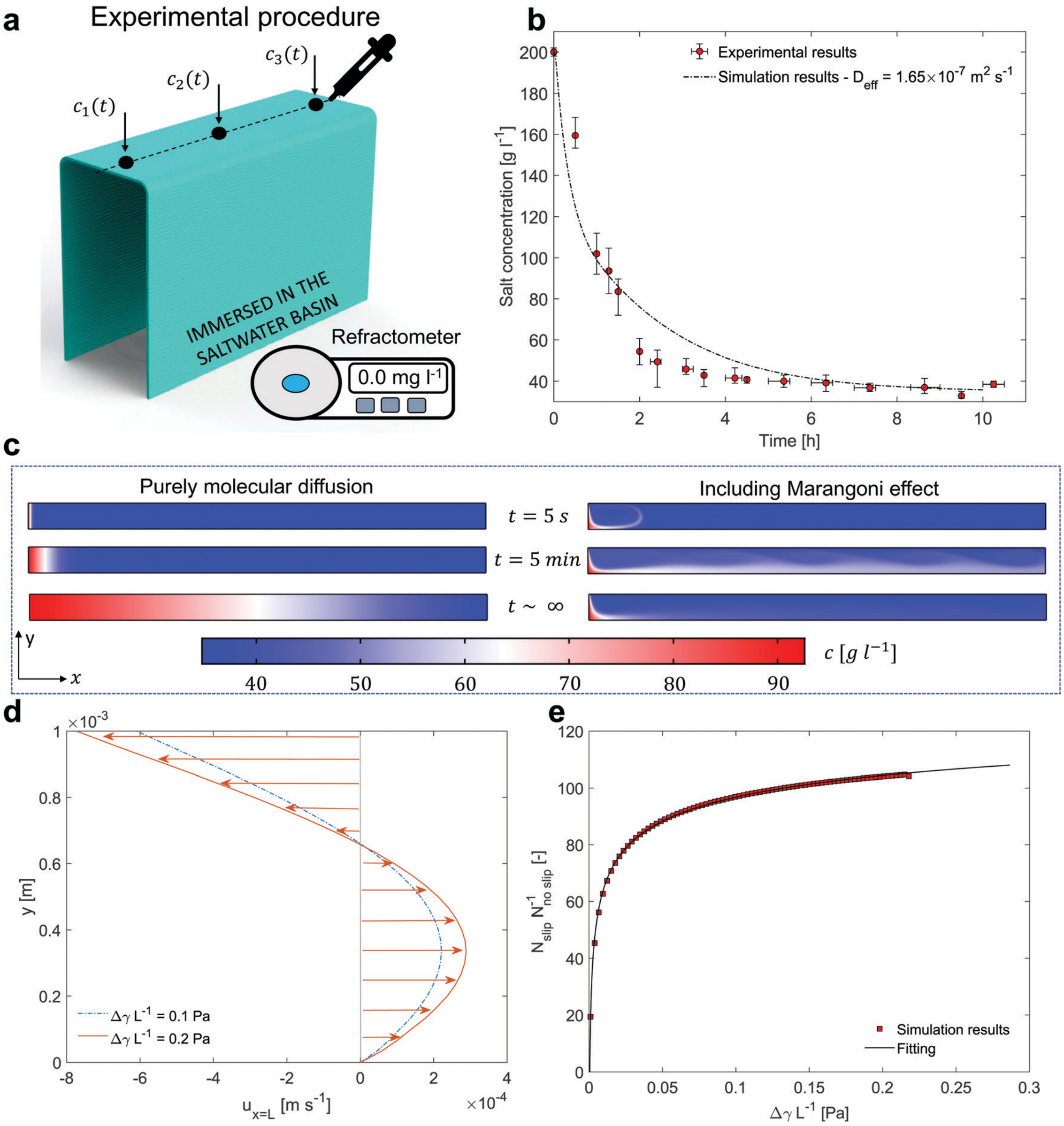

Fig. 2 Salt rejection performance. (a) Experimental setup for measuring the concentration profile over time. Black dots indicate the positions where the salt concentration is monitored. (b) Salt concentration over time. Red circles represent the experimental results, whilst the black dashed line represents the simulation results. The bars reported for each point show the minimum and maximum of the experimental measurements among the five repetitions. (c) Transient concentration surface plots. Left side: Classical molecular diffusion ($D = 1.5 \times 10^{-9}$ m^2 s^{-1}[44]). Right side: Including Marangoni effect. (d) Stationary velocity profiles at the outlet of the domain ($x = L$) and in presence of an interface are reported in case of 0.1 (*i.e.* $\Delta c = 57.5$ g l^{-1}) and 0.2 (*i.e.* $\Delta c = 115$ g l^{-1}) Pa. (e) Ratio between the outgoing molar flux in case of slip (N_{slip}, Marangoni effect) and no slip boundary condition (N_{noslip}), as function of the driving force $\Delta\gamma L^{-1}$. The resulting trend can be well fitted (R-square = 0.99) by the power function $y = ax^b + c$ (black line), being $a = -50.01$, $b = -0.16$, $c = 169.10$ the fitting parameters. The units of measure of x and y are reported in (e).

the existence of a surface tension gradient.[36] This condition can be written as:

$$\left[-p\mathbf{I} + \mu\left(\nabla\mathbf{u} + (\nabla\mathbf{u})^T\right) - \frac{2}{3}\mu(\nabla\cdot\mathbf{u})\mathbf{I}\right]\cdot\mathbf{n} = \sigma\nabla c, \tag{3}$$

where $\mathbf{n}$ is the unit normal vector and σ is the concentration derivative of the surface tension γ, namely $\sigma = \frac{\partial\gamma}{\partial c} \approx 1.76 \times 10^{-6}\ \mathrm{N\ m^{-1}}\left(\mathrm{mol\ m^{-3}}\right)^{-1}$.[42,43] On the other hand, when the purely diffusive flow is considered, a no-slip boundary condition is applied in place of eqn (3). In both cases, a Dirichlet boundary condition is applied at the left side of the simulation domain to reproduce a fixed arbitrary concentration of NaCl and the initial concentration of the entire domain is set to c_0 equal to 35 g l^{-1} (namely the seawater concentration). Details on the boundary conditions are reported in Supplementary Note 6 (ESI†).

The simulation results, after 5 seconds, 5 minutes and at stationary conditions are reported in Fig. 2c. The concentration surface plots in case of classic diffusion mechanisms and Marangoni effect are shown on the left and right side of the sub-panel, respectively. In Fig. 2d, the stationary velocity profiles that occur in the saltwater thin film at the outlet section (see Fig. 2d) are reported. Without loosing generality, the velocity profiles in case of $\Delta\gamma L^{-1}$ equal to 0.1 and 0.2 Pa are shown (see also Supplementary Note 6, ESI†).

The results show a faster mass transport process when the Marangoni effect is included in the model. In detail, the following ratio has been estimated by analysing the outgoing molar fluxes in the simulations:

$$\frac{N_{\text{slip}}}{N_{\text{no slip}}} = \frac{\int_0^{\delta_l}(-D_i\nabla c_i + \mathbf{u}c_i)_{\text{slip}}\cdot\mathbf{n}\mathrm{d}y}{\int_0^{\delta_l}(-D_i\nabla c_i)_{\text{no slip}}\cdot\mathbf{n}\mathrm{d}y}, \tag{4}$$

where N_{slip} and N_{noslip} represent the outgoing molar fluxes in case of Marangoni effect and a purely diffusive flow, respectively. In Fig. 2e, this ratio is reported as function of the driving force, namely $\Delta\gamma L^{-1}$, being L the length of the hydrophilic layer. The simulation results show that the outgoing molar flux obtained considering the Marangoni effect is more than 2 orders of magnitude larger with respect to the purely diffusive case ($D_{\text{eff}} = \frac{N_{\text{slip}}}{N_{\text{no slip}}}D$, where $\frac{N_{\text{slip}}}{N_{\text{no slip}}} \approx 110$ and $D = 1.5 \times 10^{-9}$ m^2 s^{-1}[44]).

This effective diffusion coefficient is then used to simulate the salt rejection process actually observed in the experiments, namely through a porous medium affected by gravity for the vertical portion of domain (see geometry represented in Fig. 2a). In detail, the continuity equation applied to the porous medium (with porosity ε) is written as

$$\frac{\partial(\varepsilon\rho)}{\partial t} + \nabla\cdot(\rho\mathbf{u}) = 0; \tag{5}$$

whilst, the momentum balance equation for variable density fluid flow in a porous medium, namely the Darcy's equation, can be written as

$$\mathbf{u} = -\frac{k}{\mu}(\nabla p - \rho\mathbf{g}), \tag{6}$$

where k is the permeability (1×10^{-10} m^2) of the porous medium measured experimentally by the procedure described in Supplementary Note 3 (ESI†) and p is the pressure.

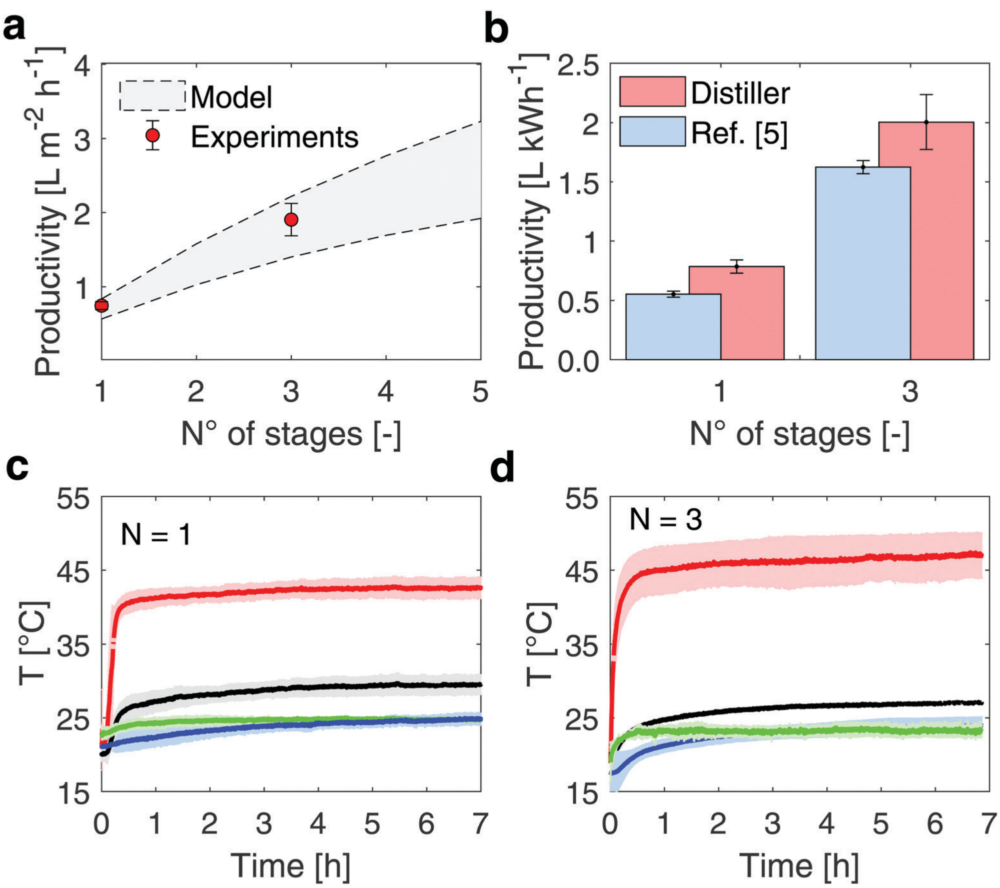

Fig. 3 Desalination performance of the modular distiller under the sun simulator. (a) The experimental performance of the device (red circles) are obtained under laboratory conditions, with 950 W m^{-2} input thermal energy. The model prediction and uncertainty are represented by the grey band (see Supplementary Note 8, ESI†). (b) Comparison between experimental desalination performance with different numbers of stages. The distillate productivity indicates the litres of distilled water produced per kWh of solar energy input. Blue and red columns are referred to ref. 5 and the here proposed distiller, respectively. The error bars depict ±1 s.d. (c) Temperature profiles during laboratory testing of the 1- and (d) 3-stage distiller, respectively. Red, black, green and blue lines refer to the top black coating, last-stage condenser, ambient and seawater basin temperatures, respectively. The color bands represent ±1 s.d.

The gravity vector is $\mathbf{g} = (0, -g)$. The transport of diluted species in a porous medium is governed by the following advection–diffusion equation:

$$\varepsilon\frac{\partial c_i}{\partial t} + \nabla\cdot\left(-\frac{\varepsilon D_{i,\mathrm{eff}}}{\tau_{\mathrm{wick}}}\nabla c_i\right) + \mathbf{u}\cdot\nabla c_i = 0, \qquad (7)$$

where $D_{i,\mathrm{eff}}$ is the effective diffusion coefficient in presence of an interface, ε is the porosity of the porous medium (the experimental procedure for evaluating this parameter is reported in Supplementary Note 3, ESI†) and τ_{wick} the tortuosity. The simulation results (see black dashed line in Fig. 2b) show consistency with the experimental ones.

It is worth pointing out that, in the tested modular device, the salt accumulation does not affect the solar absorption since it does not affect the reflection. In fact, salt deposition eventually occurs in the device without interacting with the solar beam, contrarily to what occurs in the solar vaporization structures,[8] where the evaporating and the solar absorption area coincide. In addition, no fouling or crystallization had ever encountered during experiments.

3.2 Distillate productivity

Once proven the effectiveness of the salt removal process, the distillate productivity of the device has been evaluated under different operating conditions and configurations. The experimental setup used for testing the distiller is described in Supplementary Note 7 (ESI†).

3.2.1 Laboratory conditions. The device, fed with artificial seawater (water/NaCl solution at 35 g L^{-1}), is tested by exploiting a solar simulator with solar flux set to 950 W m^{-2}.

Two configurations characterized by a different number of distillation stages (1- and 3-stages configuration device) are assembled and tested, and the experimental performance are shown in Fig. 3 together with the model predictions (see Supplementary Note 8, ESI† for details on the theoretical model). The measured specific mass flow rates (J) are 0.745 ± 0.053 L m^{-2} h^{-1} and 1.904 ± 0.219 L m^{-2} h^{-1} (mean value ±1 s.d.) in case of 1- and 3-stages configuration device, respectively (red circles in Fig. 3). In detail, four different experiments are performed over up to 8 hours (see Supplementary Note 4, ESI†) for each configuration, to ensure repeatability.

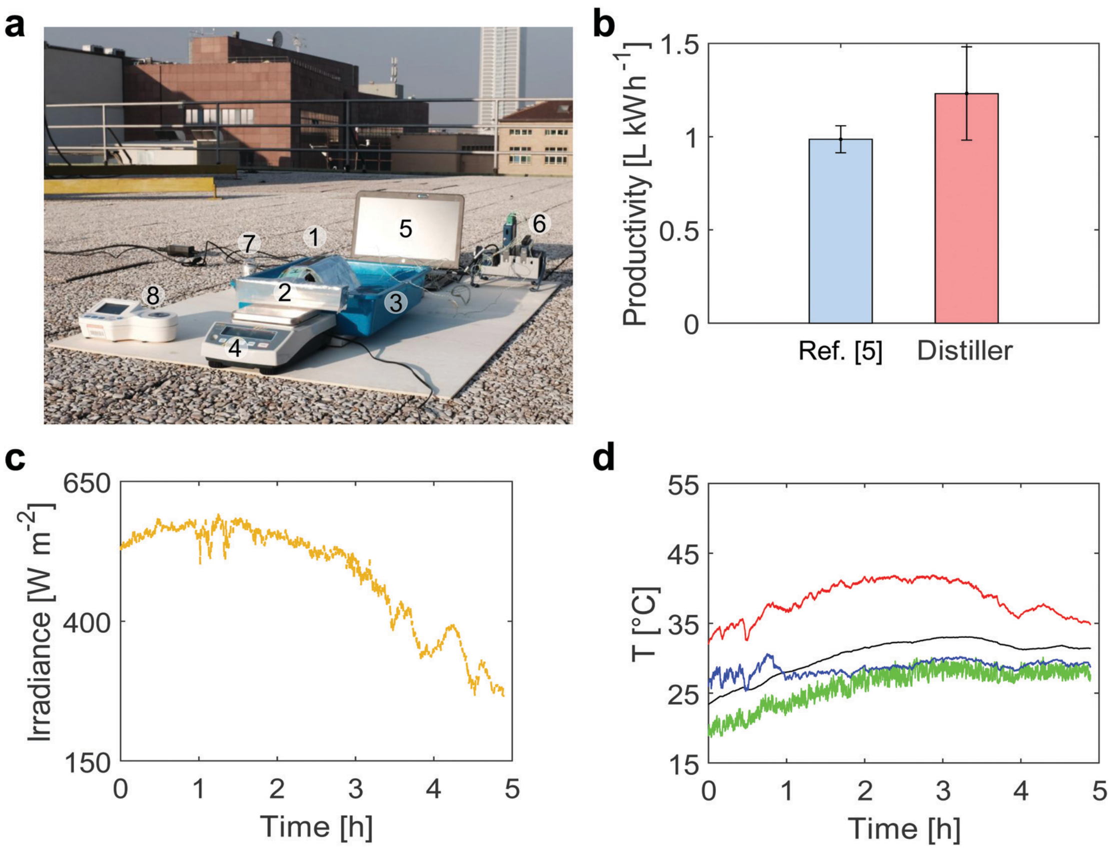

Fig. 4 Outdoor (roof) testing of the modular distiller. (a) The following components were present in the experimental tests performed on the roof of Department of Energy (Politecnico di Torino, Torino – Italy): (1) the modular distiller, (2) an output basin for the distilled water, (3) an input basin for the saltwater, (4) a scale for distillate mass measurement, (5) a laptop for data storage and elaboration, (6) a data acquisition board, (7) a pyranometer for solar irradiance measurement, (8) a digital refractometer for salinity measurement (see Supplementary Note 7, ESI†). (b) Distillate productivity under outdoor conditions (October 24th 2018, 45°03′43.0″ N 7°39′35.7″ E Torino – Italy). Error bars represent ±1 s.d. (c) Solar irradiance and (d) temperature profiles (October 24th 2018, 45°03′43.0″ N 7°39′35.7″ E Torino – Italy) during outdoor tests. Red, black, blue and green lines represent the black absorber (top side of distiller), last stage condenser (bottom side of distiller), seawater basin and ambient temperatures, respectively.

In Fig. 3b, these experimental productivities are expressed in terms of L kWh^{-1} (normalization of the distillate production by the incoming solar flux). The proposed device presents a distillate productivity enhancement of 42% in case of 1-stage configuration and 23% in case of 3-stage configuration with respect to a previous implementation of multistage passive distiller,[5] because of the optimized thickness of the air gap (see Supplementary Note 3, ESI†), while relying on a more robust and cheaper setup (see Supplementary Note 9, ESI† for further details on the costs). The GOR index (namely gained output ratio, which is defined as $\frac{J\Delta h_{\mathrm{LV}}}{q_{\mathrm{solar}}}$)[45] achieves 1.35 in case of 3-stage configuration.

In these experiments, the ambient temperature is set to 25 °C, while the temperature measured across the distiller ranges from 42.69 ± 1.27 °C at the top side of the evaporator, to 29.48 ± 1.41 °C at the bottom side of the condenser (1-stage setup, see Fig. 3c). In the 3-stage setup, the temperature ranges from 47.32 ± 2.63 °C at the top side of evaporator in the first stage, to 27.04 ± 0.21 °C at the bottom side of condenser in the third stage (see Fig. 3d).

3.2.2 **Field tests.** The 3-stage device is also tested under outdoor conditions on the roof of the Department of Energy at Politecnico di Torino (Italy). The measurements, carried out in October 24th 2018 with clear sky conditions for 5 consecutive hours, are shown in Fig. 4. An average $q_{\mathrm{solar}} = 483 \pm 94$ W m^{-2} (mean value ±1 s.d.) is measured during the test.

The produced distillate mass is gathered in a basin and monitored using a balance. Salt contamination was not observed during all the experiments. When exposed to direct sunlight, the 3-stage distiller produced 0.595 L m^{-2} h^{-1} in average (*R*-square equal to 0.905) namely 1.25 ± 0.25 L kWh^{-1}, which means a distillate productivity enhancement of 25% with respect to the value reported in ref. 5.

The experimental performance of the passive distiller tested under field conditions are also within the calculated uncertainties of the theoretical model, which depend on the variability of the outdoor conditions. In detail, the mismatch between the prediction of the theoretical model (evaluated using the mean value of each parameter reported in Table S4, ESI†) and the experimental one is equal to 13%.

4 Conclusions

Salt management remains a non-trivial issue in desalination technologies for long-term operations. Suitable strategies should be proposed to mitigate the clogging that affects the long-term stability of the current devices, thus limiting future practical applications of the technology. Furthermore, as far as passive desalination technologies are concerned, a deep understanding of the salt rejection phenomenon is extremely important to propose and develop future materials with tailored characteristics.

Here, we proposed a passive and modular distiller able to exploit the latent heat of condensation several times[5] and characterized by a smart design to minimize salt accumulation,[6] taking advantage of a novel understanding of the relationship between the salt removal process and the Marangoni effect in the desalination field. In detail, a passive rejection of the salt accumulated in the evaporator during operating conditions is obtained. The main achievement of this research work is represented by the full understanding of the phenomenon that determines these enhanced salt rejection capabilities. This phenomenon is the Marangoni effect[36] and, as far as we know, it has never been resorted and exploited to investigate the salt rejection process occurring in passive desalination technologies before.

Experiments and simulations are conducted to characterize the performance in terms of salt rejection and distillate mass flow rates. First, the salt rejection from the hydrophilic evaporator after a typical daytime distillate production is addressed and solved by optimizing the geometry of the inlet hydrophilic strips immersed in the seawater basin. In detail, the width of the hydrophilic layer is designed to increase the ratio between the discharging area, used for evacuating the salt, and the evaporating area. Noteworthy, experimental results on the salt rejection process imply that the effective diffusion coefficient is more than 2 orders of magnitude larger with respect to the classic diffusion coefficient. This mismatch is explained by resorting to the Marangoni effect at the water–air interface, which originates from the spatial gradient of the salt concentration causing the surface tension gradient. This effect speeds up the discharging process of NaCl solute. The experimental campaign demonstrates that a 75% salt concentration decrease is achieved after 2 hours.

Then, an improved stratigraphy configuration is proposed for the multistage distiller, implemented and experimentally tested. In detail, a theoretical model is used for designing the optimal thickness of the air gap which separates the evaporator from the condenser. The previously used hydrophobic microporous membranes are substituted with a simple and cheaper plastic spacer. The prototype is tested both in laboratory and under field conditions. The results confirmed a 42% and 23% increase of the produced distillate with respect to previous investigation in case of 1- and 3-stage configuration device, respectively. Considering the 3-stage configuration, it experimentally reaches a productivity, in terms of distillate flow rate, of almost 2 L m^{-2} h^{-1}. Parallel to this, a 80% cost reduction is achieved, mainly due to the replacement of the expensive membrane with the air gap. The total estimated cost is 1.3 USD for a 12 × 3.5 cm^2 device. Considering the predicted productivity (namely 6 L m^{-2} h^{-1} in case of 10-stage configuration device and two years lifetime), the estimated total cost of the produced water is around 12 USD m^{-3}, not far from the one of active desalination technologies driven by renewable energy.[46]

The high distillate yield, which is due to the ability of reusing the harvested solar energy, and the passive and efficient salt rejection, which ensures long-term stability of the performance, may lead to near-term deployment of market-ready passive desalination devices.

Further research has to be oriented towards optimized hydrophilic materials with anti-fouling properties and tailored capillary action to (i) feed a larger number of distillation stages with saltwater and (ii) guarantee an increased and optimal Marangoni-driven flow. In this way, it would be possible to further increase the productivity and to lower the cost of the desalinated water, thus increasing the competitiveness of the solar passive desalination device with respect to active technologies.

Conflicts of interest

There are no conflicts to declare.

Acknowledgements

The authors thank Gang Chen for the useful discussions. The authors thank the ''Compagnia di San Paolo'' for supporting the MISTI-MITOR projects in 2016 and 2018. M. M., M. F. and P. A. thank the CleanWaterCenter@PoliTo. E. C. and P. A. acknowledge partial support of the Italian National Project PRIN ''Heat transfer and Thermal Energy Storage Enhancement by Foams and Nanoparticles'' (2017F7KZWS).

References

1 C. J. Vörösmarty, P. Green, J. Salisbury and R. B. Lammers, Global water resources: vulnerability from climate change and population growth, *Science*, 2000, **289**, 284–288.

2 C. P. Kelley, S. Mohtadi, M. A. Cane, R. Seager and Y. Kushnir, Climate change in the Fertile Crescent and implications of the recent Syrian drought, *Proc. Natl. Acad. Sci. U. S. A.*, 2015, **112**, 3241–3246.

3 M. M. Mekonnen and A. Y. Hoekstra, Four billion people facing severe water scarcity, *Sci. Adv.*, 2016, **2**, e1500323.

4 D. Molden, *Water for food water for life: A comprehensive assessment of water management in agriculture*, Routledge, 2013.

5 E. Chiavazzo, M. Morciano, F. Viglino, M. Fasano and P. Asinari, Passive solar high-yield seawater desalination by modular and low-cost distillation, *Nat. Sustain.*, 2018, **1**, 763.

6 G. Ni, S. H. Zandavi, S. M. Javid, S. V. Boriskina, T. A. Cooper and G. Chen, A salt-rejecting floating solar still for low-cost desalination, *Energy Environ. Sci.*, 2018, **11**, 1510–1519.

7 T. A. Cooper, S. H. Zandavi, G. W. Ni, Y. Tsurimaki, Y. Huang, S. V. Boriskina and G. Chen, Contactless steam generation and superheating under one sun illumination, *Nat. Commun.*, 2018, **9**, 5086.

8 H. Ghasemi, G. Ni, A. M. Marconnet, J. Loomis, S. Yerci, N. Miljkovic and G. Chen, Solar steam generation by heat localization, *Nat. Commun.*, 2014, **5**, 4449.

9 C. Zhang, Z. Chen, Z. Xia, R. Waldman, S.-L. Wu, H.-C. Yang and S. Darling, Ferric tannate photothermal material for efficient water distillation, *Environ. Sci.: Water Res. Technol.*, 2020, **6**, 911–915.

10 W. Wang, Y. Shi, C. Zhang, S. Hong, L. Shi, J. Chang, R. Li, Y. Jin, C. Ong, S. Zhuo and P. Wang, Simultaneous production of fresh water and electricity via multistage solar photovoltaic membrane distillation, *Nat. Commun.*, 2019, **10**, 1–9.

11 M. Morciano, M. Fasano, U. Salomov, L. Ventola, E. Chiavazzo and P. Asinari, Efficient steam generation by inexpensive narrow gap evaporation device for solar applications, *Sci. Rep.*, 2017, **7**, 1–9.

12 M. Morciano, M. Fasano, L. Bergamasco, A. Albiero, M. L. Curzio, P. Asinari and E. Chiavazzo, Sustainable freshwater production using passive membrane distillation and waste heat recovery from portable generator sets, *Appl. Energy*, 2020, **258**, 114086.

13 Z. Xu, L. Zhang, L. Zhao, B. Li, B. Bhatia, C. Wang, K. L. Wilke, Y. Song, O. Labban and J. H. Lienhard, *et al.*, Ultrahigh-efficiency desalination via a thermally-localized multistage solar still, *Energy Environ. Sci.*, 2020, **13**, 830–839.

14 J. Xu, Z. Wang, C. Chang, B. Fu, P. Tao, C. Song, W. Shang and T. Deng, Solar-driven interfacial desalination for simultaneous freshwater and salt generation, *Desalination*, 2020, **484**, 114423.

15 A. K. Menon, I. Haechler, S. Kaur, S. Lubner and R. S. Prasher, Enhanced solar evaporation using a photo-thermal umbrella for wastewater management, *Nat. Sustain.*, 2020, 1–8.

16 L. Wu, Z. Dong, Z. Cai, T. Ganapathy, N. X. Fang, C. Li, C. Yu, Y. Zhang and Y. Song, Highly efficient three-dimensional solar evaporator for high salinity desalination by localized crystallization, *Nat. Commun.*, 2020, **11**, 1–12.

17 H. Tanaka, T. Nosoko and T. Nagata, Experimental study of basin-type, multiple-effect, diffusion-coupled solar still, *Desalination*, 2002, **150**, 131–144.

18 D. D. W. Rufuss, S. Iniyan, L. Suganthi and P. Davies, Solar stills: A comprehensive review of designs, performance and material advances, *Renewable Sustainable Energy Rev.*, 2016, **63**, 464–496.

19 Z. Wang, M. Han, F. He, S. Peng, S. B. Darling and Y. Li, Versatile coating with multifunctional performance for solar steam generation, *Nano Energy*, 2020, 104886.

20 Z.-J. Xia, H.-C. Yang, Z. Chen, R. Z. Waldman, Y. Zhao, C. Zhang, S. N. Patel and S. B. Darling, Porphyrin Covalent Organic Framework (POF)-Based Interface Engineering for Solar Steam Generation, *Adv. Mater. Interfaces*, 2019, **6**, 1900254.

21 H.-C. Yang, Z. Chen, Y. Xie, J. Wang, J. W. Elam, W. Li and S. B. Darling, Chinese ink: A powerful photothermal material for solar steam generation, *Adv. Mater. Interfaces*, 2019, **6**, 1801252.

22 P. Tao, G. Ni, C. Song, W. Shang, J. Wu, J. Zhu, G. Chen and T. Deng, Solar-driven interfacial evaporation, *Nat. Energy*, 2018, **3**, 1031–1041.

23 Y. Zhang, T. Xiong, D. K. Nandakumar and S. C. Tan, Structure Architecting for Salt-Rejecting Solar Interfacial Desalination to Achieve High-Performance Evaporation With *In Situ* Energy Generation, *Adv. Sci.*, 2020, **7**, 1903478.

24 F. Signorato, M. Morciano, L. Bergamasco, M. Fasano and P. Asinari, Exergy analysis of solar desalination systems based on passive multi-effect membrane distillation, *Energy Rep.*, 2020, **6**, 445–454.

25 A. Deshmukh, C. Boo, V. Karanikola, S. Lin, A. P. Straub, T. Tong, D. M. Warsinger and M. Elimelech, Membrane distillation at the water-energy nexus: limits, opportunities, and challenges, *Energy Environ. Sci.*, 2018, **11**, 1177–1196.

26 K.-T. Lin, H. Lin, T. Yang and B. Jia, Structured graphene metamaterial selective absorbers for high efficiency and omnidirectional solar thermal energy conversion, *Nat. Commun.*, 2020, **11**, 1–10.

27 F. Zhao, Y. Guo, X. Zhou, W. Shi and G. Yu, Materials for solar-powered water evaporation, *Nat. Rev. Mater.*, 2020, 1–14.

28 L. Zhang, Z. Xu, B. Bhatia, B. Li, L. Zhao and E. N. Wang, Modeling and performance analysis of high-efficiency thermally-localized multistage solar stills, *Appl. Energy*, 2020, **266**, 114864.

29 S. Suneja and G. Tiwari, Optimization of number of effects for higher yield from an inverted absorber solar still using the Runge-Kutta method, *Desalination*, 1998, **120**, 197–209.

30 Z. Wang, T. Horseman, A. P. Straub, N. Y. Yip, D. Li, M. Elimelech and S. Lin, Pathways and challenges for efficient solar-thermal desalination, *Sci. Adv.*, 2019, **5**, eaax0763.

31 Y. Pang, J. Zhang, R. Ma, Z. Qu, E. Lee and T. Luo, Solar-Thermal Water Evaporation: A Review, *ACS Energy Lett.*, 2020, **5**, 437–456.

32 S. He, C. Chen, Y. Kuang, R. Mi, Y. Liu, Y. Pei, W. Kong, W. Gan, H. Xie and E. Hitz, *et al.*, Nature-inspired salt resistant bimodal porous solar evaporator for efficient and stable water desalination, *Energy Environ. Sci.*, 2019, **12**, 1558–1567.

33 Y. Xia, Q. Hou, H. Jubaer, Y. Li, Y. Kang, S. Yuan, H. Liu, M. W. Woo, L. Zhang and L. Gao, *et al.*, Spatially isolating salt crystallisation from water evaporation for continuous solar steam generation and salt harvesting, *Energy Environ. Sci.*, 2019, **12**, 1840–1847.

34 Y. Shi, C. Zhang, R. Li, S. Zhuo, Y. Jin, L. Shi, S. Hong, J. Chang, C. Ong and P. Wang, Solar evaporator with controlled salt precipitation for zero liquid discharge desalination, *Environ. Sci. Technol.*, 2018, **52**, 11822–11830.

35 V. Kashyap, A. Al-Bayati, S. M. Sajadi, P. Irajizad, S. H. Wang and H. Ghasemi, A flexible anti-clogging graphite film for scalable solar desalination by heat localization, *J. Mater. Chem. A*, 2017, **5**, 15227–15234.

36 H. Kitahata and N. Yoshinaga, Effective diffusion coefficient including the Marangoni effect, *J. Chem. Phys.*, 2018, **148**, 134906.

37 M. G. Velarde and R. K. H. Zeytounian, *Interfacial phenomena and the Marangoni effect*, Springer, 2002.

38 K. Mills, B. Keene, R. Brooks and A. Shirali, Marangoni effects in welding, *Philos. Trans. R. Soc. London, Ser. A*, 1998, **356**, 911–925.

39 P. Lee, P. Quested and M. McLean, Modelling of Marangoni effects in electron beam melting, *Philos. Trans. R. Soc. London, Ser. A*, 1998, **356**, 1027–1043.

40 H. C. Kuhlmann, *Thermocapillary convection in models of crystal growth*, Springer, 1999.

41 H. Hu and R. G. Larson, Marangoni effect reverses coffee-ring depositions, *J. Phys. Chem. B*, 2006, **110**, 7090–7094.

42 K. G. Nayar, D. Panchanathan, G. H. McKinley and J. H. Lienhard, Surface tension of seawater, *J. Phys. Chem. Ref. Data*, 2014, **43**, 043103.

43 M. H. Sharqawy, J. H. Lienhard and S. M. Zubair, Thermophysical properties of seawater: a review of existing correlations and data, *Desalin. Water Treat.*, 2010, **16**, 354–380.

44 V. Vitagliano and P. Lyons, Diffusion Coefficients for Aqueous Solutions of Sodium Chloride and Barium Chloride, *J. Am. Chem. Soc.*, 1956, **78**, 1549–1552.

45 V. G. Gude, Exergy evaluation of desalination processes, *ChemEngineering*, 2018, **2**, 28.

46 A. Al-Karaghouli and L. L. Kazmerski, Energy consumption and water production cost of conventional and renewable-energy-powered desalination processes, *Renewable Sustainable Energy Rev.*, 2013, **24**, 343–356.